Understanding the structure directing action of copper-polyamine complexes in the direct synthesis of Cu-SAPO-34 and Cu-SAPO-18 catalysts for the selective catalytic reduction of NO with NH_3

Alessandro Turrina,[1] Eike C. V. Eschenroeder,[1] Bela E. Bode,[1] Jillian E. Collier,[2] David C. Apperley,[3] Paul A. Cox,[4] John L. Casci,[5] Paul A. Wright[1*]

[1] EaStCHEM School of Chemistry and Centre of Magnetic Resonance, University of St Andrews, Purdie Building, North Haugh, St Andrews, KY169ST, United Kingdom.

[2] Johnson Matthey Technology Centre, Reading, RG4 9NH, United Kingdom.

[3] Department of Chemistry, Durham University, South Road, Durham DH1 3LE, United Kingdom.

[4] School of Pharmaceutics and Biomedical Sciences, University of Portsmouth, St. Michael's Building, White Swan Road, Portsmouth, PO1 2DT, United Kingdom.

[5] Johnson Matthey, Chilton PO Box 1, Belasis Avenue, Billingham, TS23 1LB, United Kingdom.

[*] Corresponding author. Tel.: +44 1334 463793; fax: +44 1334 463808. E-mail address: paw2@st-andrews.ac.uk (P.A. Wright).

Abstract

Cu^{2+} cations complexed by linear polyamines have been studied as structure-directing agents (SDAs) for the direct synthesis of copper-containing microporous silicoaluminophosphate (SAPO) materials. The complexing ligands diethylenetriamine (DETA), N-(2-hydroxyethyl)ethylenediamine (HEEDA), triethylenetetramine (TETA), N,N′-bis(2-aminoethyl)-1,3-propanediamine (232), 1,2-bis(3-aminopropylamino)ethane (323), tetraethylenepentamine (TEPA) and pentaethylenehexamine (PEHA) have been investigated. For comparison, syntheses have been performed using the analogous nickel-polyamine complexes. Cu^{2+} and Ni^{2+} forms of both SAPO-18 and SAPO-34 materials have been prepared. While most polyamine complexes direct crystallisation to SAPO-34, SAPO-18 has been prepared with Cu^{2+}(232), Ni^{2+}(232) and Ni^{2+}(TETA). The coordination geometry of the included metal complexes was studied by UV-visible and EPR spectroscopy and computer simulation. SAPO-18 is favoured by the smaller square planar complexes or octahedral species (with 2 water molecules) of 232 and TETA. Calcination leaves extra-framework Cu^{2+} and Ni^{2+} cations within SAPO-18 and SAPO-34 frameworks. *In situ* synchrotron IR spectroscopy of Ni-SAPO-18 has shown thermal template degradation occurs via nitrile intermediates. Rietveld structural analysis located extra-framework Cu^{2+} and Ni^{2+} cations released by calcination. In SAPO-34, Cu^{2+} and Ni^{2+} were located in the 8R window of the *cha* cage. A second site was found for Ni^{2+} at the centre of the six-membered rings (6Rs) of the double-six-ring (D6R) sub-units. In SAPO-18 both Cu^{2+} and Ni^{2+} cations were located only in the 6Rs of the D6R sub-units. Selected copper SAPO-18 and SAPO-34 samples were tested in the selective catalytic reduction of NO with ammonia (NH_3-SCR); both showed high activity.

Keywords: One-pot synthesis, Metal- polyamine complexes, Cu-SAPO-34, Cu-SAPO-18, NH_3-SCR

1. Introduction

Small pore zeolites and silicoaluminphosphates (SAPOs) with Cu^{2+} cations in extra-framework positions show excellent activity in the selective catalytic reduction (SCR) of NO with NH_3, an important conversion for the abatement of pollution from lean burn engines. [1] Materials with the CHA and AEI topology types (zeolites SSZ-13 [2] and SSZ-39 [3] and SAPOs-34 [4] and -18, [5] respectively) are among the most intensely studied for this reaction, (Figure 1). Cu^{2+} cations can be introduced into the solids by cation exchange of materials from which the original alkylammonium structure directing agents have been removed by calcination. As well as requiring a separate preparative step, this can lead in SAPOs to a reduction in crystallinity and an inhomogeneous distribution of Cu^{2+} cations. Recently, we and others have developed a synthetic approach that utilises copper-polyamine complexes as templates, which enables the direct inclusion of complexed Cu^{2+} cations in the solids. [6-12] Calcination then releases the Cu^{2+} cations to extra-framework sites distributed throughout the crystals and removes the need for a cation-exchange step. This process was first demonstrated for SAPO STA-7, [6] and subsequently for SSZ-13, [7] SAPO-34, [9-11] and very recently for SAPO-18 [12] giving active, selective and hydrothermally stable catalysts. The details of the mechanism by which the calcination of the complex-bearing precursor to SAPO STA-7 gives a porous, acidic framework with dispersed copper cations has been followed by *ex situ* UV-visible spectroscopy and by *in situ* microcrystal IR spectroscopy. [13] Further, the locations of Cu^{2+} cations in calcined Cu SAPO STA-7 have been determined by Rietveld refinement against powder X-ray diffraction data to be in six-membered ring (6R) sites and eight-membered ring (8R) sites of the STA-7 structure.

Most interest in Cu^{2+}-zeotype catalysts for SCR centres on zeolites and SAPOs with the CHA framework topology, because of their high porosity and catalytic activity and the relative ease of their synthesis. We and others [9-11] have shown that the copper complexes of the linear polyamines triethylenetetramine and tetraethylenepentamine are suitable SDAs for SAPO-34, and that calcination gives active SCR catalysts. Linear polyamines are relatively affordable (compared to the azamacrocycle used in the synthesis of Cu-SAPO STA-7) so we set out to investigate the action of a range of copper complexes of the linear polyamines in the direct synthesis of Cu^{2+}-containing SAPOs, and to understand the mechanism by which they direct crystallisation. The linear polyamines used, together with their acronyms, are shown in Scheme 1. All except 232 were found to give Cu SAPO-34 in the presence of Cu^{2+}.

In addition to the preparation of different Cu^{2+}-containing SAPO-34 materials, it was possible with specific metal polyamine complex SDAs and under a restricted range of gel compositions to direct the synthesis towards Cu-SAPO-18. SAPO-18, like its polytype SAPO-34, is a small pore structure composed entirely of D6R building blocks, linked by 4Rs. The difference between the two structures lies in the mode of stacking of layers of D6Rs: in the CHA topologies all D6Rs have the same orientation whereas in AEI the structure consists of layers of D6Rs with alternating orientations (Figure 1). Very recently, the direct synthesis of copper-complex containing SAPO-18 has been reported for the first time, where the preparation requires the addition of dimethylpiperidinium cation as the template and the Cu TETA complex is included as a 'co-template' in the *aei* cages of SAPO-18 crystals. Here, we show that the copper complex of '232' has a direct templating action towards the SAPO-18 structure.

In all the Cu-SAPO-34 and Cu-SAPO-18 materials reported here, the Cu-polymaine complex has a strong templating action. To understand this better, a detailed

spectroscopic study (UV-visible, EPR) of the encapsulated complexes was performed to determine their geometry and hydration state. Additionally, Ni^{2+} complexes of the same set of polyamines were examined in a parallel set of experiments to give more information on the role of the complex's geometry in controlling crystallisation in these systems. Ni^{2+} DETA complexes have previously been shown to act as SDAs in aluminophosphate syntheses. [14,15] Both Ni-SAPO-34 and Ni-SAPO-18 materials crystallised (reported here for the first time) and in addition to spectroscopic characterisation, modelling was used to explain the observed phase selectivity.

Calcination of the different solids gave Cu- and Ni- forms of both SAPO-34 and SAPO-18. The calcination of Ni-SAPO-18 was followed *in situ* by Synchrotron radiation (SR) IR microspectroscopy and the final location of Cu^{2+} and Ni^{2+} cations in the calcined forms of both SAPO-34 and SAPO-18 were determined by Rietveld refinement. Selected calcined Cu-SAPO-18 and Cu-SAPO-34 materials were tested as catalysts for NH_3 SCR of NO and found to be active.

2. Experimental details

2.1. Synthesis and preparation

The polyamines diethylenetriamine (DETA), N-(2-hydroxyethyl)ethylenediamine (HEEDA), triethylenetetramine (TETA), N,N′-bis(2-aminoethyl)-1,3-propanediamine (232), 1,2-bis(3-aminopropylamino)ethane (323), tetraethylenepentamine (TEPA) and pentaethylenehexamine (PEHA) have been used as chelating agents with Cu^{2+} and Ni^{2+} for the synthesis of SAPO-34 and SAPO-18. In a typical preparation, fumed silica was added to an aluminophosphate gel prepared by mixing $Al(OH)_3 \cdot H_2O$ (Aldrich, technical grade) with H_3PO_4 (BDH, 85%) in water, followed by addition of the copper or nickel

complex, pre-prepared by adding copper acetate or nickel acetate to an aqueous solution of the polyamine. A portion of the total water content was set aside for this purpose. Finally an excess of the same polyamine (so that the polyamine / M^{2+} ratio was 3.5 / 1) was added dropwise to adjust the gel pH to 7. Initial synthetic attempts were made using the gel composition $Al(OH)_3$: 0.8 H_3PO_4 : 0.2 SiO_2 : 40 H_2O : 0.1 M^{2+} : 0.1 polyamine, but these gave poorly crystalline materials. Improved product crystallinity was obtained using an overall gel composition of $Al(OH)_3$: 0.61 H_3PO_4 : 0.2 SiO_2 : 40 H_2O : 0.06 Cu^{2+} (0.1 Ni^{2+}): 0.2 polyamine. This resulted in some cases in the co-crystallisation of a fine grained aluminophosphate by-product, which could be removed by sonicating the product suspension and decanting.

Cu-SAPO-18 has been prepared adopting specific conditions. Cu^{2+}-N,N′-bis(2-aminoethyl)-1,3-propanediamine (232) has been used as the SDA while tetraethylammonium hydroxide (TEAOH), was added dropwise to adjust the gel pH to 7. The overall gel composition is $Al(OH)_3$: 0.61 H_3PO_4 : 0.2 SiO_2 : 40 H_2O : 0.06 Cu-232 : 0.27 TEAOH. Seeds of STA-7, 1% weight in respect to the SiO_2 content, were added to promote the nucleation of pure SAPO-18. Details are given in Table 1. STA-7 was chosen because it has one crystal face (100) structurally similar to one of SAPO-18 (110) and none in common with SAPO-34, and overgrowths of SAPO-18 on SAPO STA-7 have been reported. [16]

The final gels were stirred continuously at room temperature until homogeneous, prior to being transferred to a Teflon-lined stainless steel autoclave and heated at 190 °C for 6 days. The resultant products were suspended in water and sonicated to force separation of crystalline material from fine grained amorphous solid, which was removed by decanting. The crystalline materials were collected by filtration, washed with deionized H_2O, and dried in air at 80 °C for 12 hours.

2.2. Characterisation

For phase identification, X-ray powder diffractograms in the 2θ range 5–50° (step size 0.01°, time step^{-1} 160 s, 0.04 rad Soller, 45 kV, 35 mA) were carried out on a Panalytical Empyrean automated diffractometer equipped with a X'Celerator detector. The data were collected in Bragg-Brentano geometry, using Cu $K_{\alpha 1}$ (λ = 1.54056 Å) X-radiation via a primary monochromator. For structure refinement, samples were loaded in 0.5 or 1.0 mm quartz glass capillaries and dehydrated at 250 °C under a vacuum of 10^{-5} mbar for 10 hours before being sealed and mounted on the diffractometer. X-ray powder diffractograms in the 2θ range 3–70° (step size 0.1°, time step^{-1} 80 s, 40 kV, 35 mA) were measured at 21 °C in Debye-Scherrer mode on a Stoe STADI/P diffractometer with a primary monochromator, using Cu $K_{\alpha 1}$ X-radiation (λ = 1.54056 Å) and equipped with a linear PSD detector.

Scanning electron microscopy was carried out with a JEOL JSM 6700F SEM with an Oxford INCA Energy 200 EDX analyser to determine the Si, Al, P, Cu and Ni content. When necessary, samples were ground fine prior to analysis, to minimise the effects of zoning on the measured compositions. More accurate determination of transition metal content was performed using a Philips PV 9400 X atomic absorption spectrometer with a Unicam hollow cathode lamp, at the characteristic resonance line, using an air-acetylene flame. Thermogravimetric analysis of as-prepared samples was performed on a NETZSCH TG1000M in a dry air flow with a heating rate of 5 °C min^{-1}. Elemental analysis was carried out by Elemental Analysis Service, London Metropolitan University, United Kingdom.

2.3. Spectroscopies

In order to understand the structure directing role of the various metal complexes, UV-visible and EPR spectroscopies were used to investigate the geometry of the coordination of the metal cations. UV-visible absorption spectra of as-prepared solid samples were measured on a JACSO V-650 UV-visible spectrophotometer equipped with a photomultiplier tube detector. Spectra were collected over the wavelength range 200–900 nm with a bandwidth of 5.0 nm and at a rate of 200 nm min^{-1}. All the samples have been measured as-prepared and after dehydration at 170 °C in a tube furnace under flowing N_2 to establish whether water molecules are present in the coordination sphere of the metal cations in the as-prepared form. EPR spectra were obtained with a Bruker EMX spectrometer operating at 9.7 GHz with 100 kHz modulation. Selected as-prepared samples and their calcined form were contained in 4 mm OD quartz tubes (Wilmad lab-glass). Spectra were recorded using a 150 mT field sweep centred at 325 mT with 2048 points resolution, a time constant and conversion time of 40.96 ms each, a modulation amplitude of 0.1 mT and a microwave power of 20 mW. As-prepared samples contained in 4 mm OD quartz tubes have been dehydrated at 170 °C under a vacuum of 10^{-5} mbar for 10 hours before being sealed and mounted on the spectrometer. Anisotropic continuous-wave (CW) spectra were fitted in EasySpin [17] from an axial *g*-tensor and assuming a collinear axial Cu-hyperfine coupling and an isotropic line width. A second component was added when this improved the fit substantially.

To determine the coordination geometry and distribution of Al, Si and P framework cations, solid-state NMR spectra were collected at room temperature using a Varian VNMRS 400 spectrometer, equipped with a widebore 14.1 T magnet, yielding Larmor frequencies of 104.2 MHz for ^{27}Al, 161.9 MHz for ^{31}P, and 79.4 MHz for ^{29}Si. Samples were dehydrated overnight at 150 °C before being packed in 4 mm ZrO_2 rotors and

rotated at a rate of 12.8 or 13.5 kHz for ^{27}Al, and 6.8 kHz for ^{31}P and ^{29}Si. Chemical shifts were recorded in ppm relative to 1 M $Al(NO_3)_3$ (aq) for ^{27}Al, 85% H_3PO_4 for ^{31}P, and TMS for ^{29}Si. All spectra were recorded with a one-pulse sequence (direct extinction) and a repeat interval of 10.0 ms (^{27}Al), 15 or 20.0 ms (^{31}P), 30 ms (^{29}Si), and a spectral width of 416.7 kHz (^{27}Al), 100.0 kHz (^{31}P), 40.3 kHz (^{29}Si).

In situ synchrotron IR microcrystal spectroscopy was used to follow the template removal from Ni-SAPO-18 single crystals, following the method of Eschenroeder and co-workers. [13] The experiments were carried out at beamline B22 at the Diamond Light Source, Didcot, UK. [18] A Bruker Vertex 80v Vacuum-FTIR equipped with a Hyperion 3000 IR microscope was set-up to a resolution of 4 cm^{-1} at 20× magnification in transmission mode with an aperture of 15×15 μm^2. A total of 256 scans per spectrum were collected at 80 kHz FTIR scanner velocity. The sample was loaded onto the bottom CaF_2 window (of two) in a Linkam FTIR600 environmental cell, continuously flushed with dry air, and mounted on the remote-controlled microscope stage operated by the OPUS software suite. [19] Absorption spectra were calculated by subtracting the corresponding background.

2.4. Computational modelling

Molecular modelling studies were performed using the Forcite module within the program Materials Studio version 6.1. [20] The Universal Force Field (UFF) was used and the charges on the framework were scaled so that a neutral simulation box was maintained upon introduction of Ni complex with a +2 charge. The framework structures were simulated using a fully aluminophosphate model with an aluminium to phosphorus ratio of 1:1; these atoms were held rigid throughout the simulation. Energy

minimisation was performed following a simulated annealing protocol that ran for 100,000 steps at temperatures of 477 °C, 227 °C, 27 °C and -173 °C. The time step used was 1 x 10^{-15} s.

2.5. Calcination and catalysis

Detemplation of selected samples was performed in a tube furnace at 550 °C (reached via a heating ramp of 20 °C min^{-1}), for 12 hours in a steam of dry oxygen. To establish the porosity of the calcined solids, adsorption isotherms for N_2 at -196 °C have been measured using a Micromeritics Tristar II 3020 apparatus on samples dehydrated under vacuum at 150 °C.

The activity of the samples for the selective catalytic reduction of NO_x using NH_3 as the reductant was tested in a fixed bed reactor. Each catalyst (0.4 g) was pelletised and then broken up to given a particle size of 250–355 μm. The reaction gas composition used was 350 ppm NO, 385 ppm NH_3, 10% O_2, 4.5% H_2O, 4.5% CO_2 and balanced by N_2. The flow rate was set at 1.3 L min^{-1}, corresponding to a weight hourly space velocity (WHSV) of 195 L $(g_{cat}\ h)^{-1}$ over the catalysts. The catalysts were introduced in the reactor and heated from 150 to 550 °C with a heating rate of 5 °C min^{-1}. Inlet and outlet gas compositions were measured using a FTIR analyser while O_2 concentrations were determined by using an O_2 analyser. To determine the hydrothermal stability of the catalysts after an extremely high temperature exposure, a separate set of pelletised samples were heated to 900 °C at a heating rate of 10 °C min^{-1} and kept there for 1 h in a flow reactor with a gas containing 4.5% H_2O in air at a flow rate of 1.3 L min^{-1}, prior to examination as a catalyst.

2.6. Crystallography: Rietveld refinemnet

Rietveld refinement of selected calcined and dehydrated copper and nickel SAPO-34 and SAPO-18 structures was carried out using the GSAS suite of programs and the EXPGUI graphical interface. [21] In the refinements the background curves were fitted by using a Chebyschev function with 30 (Cu-SAPO-34 and Ni-SAPO-34), 24 (Cu-SAPO-18) and 22 (Ni-SAPO-18) terms. A Pseudo-Voigt function (type 4) [22] was used to model the Bragg peak profiles. The framework Al-O, P/Si-O, O-O(Al), and O-O(P/Si) distances were restrained to 1.72 Å (σ = 0.025 Å), 1.51 Å (σ = 0.025 Å), 2.82 Å (σ = 0.025 Å), and 2.48 Å (σ = 0.025 Å), respectively. The isotropic atomic displacement parameters of the atoms have been constrained in groups for the tetrahedral sites and transition metals (Al, P, Cu or Ni) and O atoms respectively. In order to take into account the small impurity of SAPO-34 present in both SAPO-18 samples, a second phase was added during the refinement. Only the scale factor, the cell parameters, the peak shape and no structural parameter were refined for this second phase. The SAPO-34 fraction determined corresponds to 17.5% for Cu-SAPO-18 and 5.8% for Ni-SAPO-18. Difference Fourier analysis and iterative refinement of positions and occupancies were adopted to locate the transition metal cations within SAPO-34 and SAPO-18.

3. Results and Discussion

3.1. Synthesis and composition of Cu, Ni SAPO-34 and SAPO-18

The structure-directing role of a wide range of linear polyamine complexes of Cu^{2+} and Ni^{2+} has been investigated in the synthesis of silicoaluminophosphates. As shown in Figure 2, Figure 3 and Table 1, most of the metal complexes give SAPO-34 as product.

However, under specific conditions, for Cu^{2+} in the presence of 232 and TEA^{+} and for Ni^{2+} with 232 or TETA, SAPO-18 was obtained. All the preparations of SAPO-18 contain a very small impurity of CHA. Furthermore using only TEA^{+} as the SDA and copper acetate without polyamines, the presence of copper oxide (CuO) has been detected in the resultant SAPO-34 by PXRD (Figure S1, Supporting information). This result proves the important roles played by the linear polyamines for the incorporation of isolated metal cations.

Cu-SAPO-18 crystallised when TEAOH was used as a co-base and in the presence of seeds of STA-7, which favour its nucleation. [16] In the absence of TEA^{+} no crystalline phase was obtained, while without seeds the impurity of SAPO-34 is greatly increased (Figure S2). By contrast, Ni-SAPO-18 can be prepared using 232 or TETA as added amines without additional SDAs, and AEI/CHA intergrowths result for Ni^{2+} plus PEHA (and mixtures of 232 and TEA^{+}) (Figure 3). From this it is clear that Cu^{2+} and particularly Ni^{2+} complexes of 232 have the highest tendency of all the complexes examined to direct the crystallisation to SAPO-18, and that Ni^{2+} complexes are stronger templates for the AEI topology than Cu^{2+} complexes.

Attempts to synthesise copper and nickel SAPO-18 using a more conventional gel composition ($Al(OH)_3$: 0.8 H_3PO_4 : 0.2 SiO_2 : 40 H_2O : 0.1 M^{2+}-232) resulted in the formation of SAPO-34 when adding both Cu-232 and TEAOH, while SAPO-18 was still obtained with Ni-232 (Figure S3).

The samples' compositions and their metal content are summarised in Table 2. Approximately 0.8 copper and 1.2 nickel cations per CHA (SAPO-34) unit cell (i.e. 0.27 and 0.40 cations in each of the three *cha* cages per unit cell) and 1.2 copper and 1.8 nickel per AEI (SAPO-18) unit cell, (i.e. 0.30 and 0.45 cations in each of the four *aei* cages per unit cell) were incorporated in the presence of most of the ligands. The only

exceptions were Cu-HEEDA and Ni-232, where the higher values of 1.1 Cu^{2+} and 2.5 Ni^{2+} cations, have been measured per CHA and AEI unit cell, respectively. In the presence of 323 only 0.2 Cu^{2+} cations were incorporated within the unit cell of SAPO-34.

Not all products obtained using the various metal complexes have the same degree of crystallinity. In some cases it was necessary to sonicate aqueous suspensions before filtration to remove amorphous material. The non-stoichiometric composition of the gel ((Si+P)<Al) and the imperfect fit of the different complexes within the *cha* and *aei* cages are likely to be responsible. As reported previously, it is possible to improve the crystallinity by partially replacing the metal complex with an amine or a quaternary ammonium cation well established as SDAs for the synthesis of SAPO-34 or SAPO-18 (e.g. diethylamine, TEA^+ or N,N-dimethyl-3,5-dimethylpiperidinium cations). [9,10,12]

Figure 4 shows the crystal morphologies of Cu- and Ni-forms of both SAPO-34 and SAPO-18 synthesised in the presence of DETA and 232, respectively. Both Cu- and Ni-SAPO-34 crystals show a well-defined cubic morphology with sides of average lengths of 50 and 30 μm, respectively. Cu-SAPO-18 crystals are parallelepipeds, 8 × 8 × 3 μm, stacked and interpenetrated, while Ni-SAPO-18 crystals have an uneven cuboidal morphology with an average side of length 50 μm. EDX analysis suggests that the amorphous particles present on the crystals' surface consist of Al, P and O.

3.2. Spectroscopic characterisation of copper and nickel complexes

Evidence for the integrity of the copper and nickel complexes in the final solids, apart from their characteristic colours (Table 3), was obtained from their UV-visible spectra, which show characteristic d–d transitions (Figure 5 and Figure 6). Typical λ_{max} values

for Cu^{2+} and Ni^{2+} complexes with different coordination geometries are reported in Table S1.

Cu^{2+} complexed by DETA, TEPA and PEHA shows an absorption band around 680 nm characteristic of Cu^{2+} in octahedral coordination geometry. [23] The broad features of the Cu-TEPA spectra might be caused by the simultaneous presence of both octahedral and square pyramidal (pentacoordinate) conformations. The λ_{max} at 602 nm and 615 nm respectively for Cu-TETA and Cu-HEEDA can be attributed to a distorted square planar conformation. [23] Cu-323 shows only a weak band at 350 nm while Cu-232 exists as a square planar complex (λ_{max} = 545 nm) [23] within SAPO-18. This different observed complex geometry suggested why Cu-SAPO-18 crystallised only in the presence of Cu-232.

Considering the UV-visible spectra of nickel complex-containing SAPOs, it appears that only octahedrally coordinated Ni^{2+} species (λ_{max} = 350, 550 and 910 nm) are present in the presence of DETA, where the complex is likely to be present as $[Ni(DETA)_2]^{2+}$, in line with previous studies. [14] A similar Ni^{2+} : ligand ratio of 1 : 2 is expected for HEEDA, where a similar absorption spectrum is observed, with an additional band at 620 nm which has previously been assigned to 5-coordinate Ni^{2+}. [24] Ni^{2+}-TETA, Ni^{2+}-TEPA and Ni^{2+}-PEHA also give spectra consistent with octahedral Ni^{2+} coordination, suggesting that, at least for the first two, H_2O is also involved in the coordination sphere. By contrast, Ni^{2+}-232 and Ni^{2+}-323 show bands consistent with a mixture of octahedral and square planar (λ_{max} = 445 nm) coordination geometries. [25]

To investigate whether water molecules are present in the coordination sphere of Cu^{2+} and Ni^{2+} complexes, UV-visible spectra were measured on samples dehydrated at 170 °C in a N_2 flow (conditions that do not lead to degradation of the organic ligands). As shown in Figure 5 and summarised in Table 3 the dehydration process affected the

spectra of Cu-DETA, Cu-HEEDA and Cu-PEHA; the absorption band at 350 nm is increased, possibly due to the removal of the copper cations from complexes. Upon dehydration, Ni-TETA converts from octahedral (planar polyamine and two axial water molecules) to square planar geometry (band maximum at 445 nm) and Ni-232 shows a variation in the spectrum that can be attributed to the removal of water molecules during dehydration. The red-shift highlighted with Ni-TEPA might be associated with the removal of one molecule of water from the coordination sphere of nickel and/or a distortion of the octahedral configuration (Figure 6).

In previous papers reporting the direct synthesis of Cu-SSZ-13, [7] Cu-SAPO-34 [9-11] and Cu-SAPO-18 [12] using Cu^{2+} complexes with linear polyamines (TEPA and TETA) the UV-visible spectra reported for the as-prepared materials show a strong absorption band in the near UV region (≈ 260 nm) like ours but weak d-d transitions in the visible region. The 260 nm band might be assigned to LMCT between the framework O and isolated Cu^{2+} cations. Our UV-visible spectra show the d-d transitions much more clearly, confirming direct inclusion of the metal-polyamine complexes.

The main difference between the method of synthesis in this work from that of Corma and co-workers, [12] is that whereas a template, N,N-dimethyl-3,5-dimethylpiperidinium, is used in that work to direct the synthesis of the SAPO-18, entraining Cu^{2+} and/or Cu^{2+} complex at the same time, in our synthesis it is the Cu-232 complex that directs crystallisation of the AEI structure.

Our results indicate that the length and flexibility of the polyamines, the different metal/ligand ratio and the presence of water molecules are factors that affect the coordination geometries shown by Cu^{2+} and Ni^{2+} complexes and as a consequence the templating role of their polyamine complexes for SAPOs. Although SAPO-34 and SAPO-18 have very similar framework densities and the *cha* and *aei* cages enclose

similar volumes and are of similar lengths, their shapes are very different. While the *cha* cage is shaped like a cylinder, the *aei* cage is shaped like a pear (Figure 7). Careful analysis of the complexes reveals that SAPO-18 was obtained when the metals are in a square planar configuration or octahedral (or square pyramidal) with four planar N and one or two axial water molecules. The only exception is Ni-323, which despite having a coordination geometry similar to Ni-232 always gives SAPO-34. We speculate that this is due to the overall larger size of the complex. In order to investigate in more detail the role played by the coordination geometry of the metal-polyamine complexes in the formation of CHA and AEI, square planar $[Ni\text{-}232]^{2+}$ and octahedral $[Ni\ (DETA)_2]^{2+}$ complexes were modelled in both cages.

Energy-minimised locations of these complexes are shown in Figure 8. $[Ni\ (DETA)_2]^{2+}$ gives a binding energy of -188.78 kcal mol^{-1} within the *cha* cage which is more favourable than the -168.70 kcal mol^{-1} calculated for the *aei* cage, where the nickel complex appears to be slightly too big; it protrudes from the cage and there is close contact with the atoms of the framework. By contrast, $[Ni\text{-}232]^{2+}$ has a better binding energy inside the *aei* cage than the *cha* one, -175.31 kcal mol^{-1} cf. -155.21 kcal mol^{-1}. $[Ni\text{-}232]^{2+}$ seems to be slightly too small for the *cha* cage while the pear shape of the *aei* cage matches well with the shape of the template and may allow the presence of water molecules coordinated axially to the metal cation, giving rise to the mixture of square planar and octahedral complexes observed in the UV-visible spectra.

Electron paramagnetic resonance spectroscopy was used to obtain additional information on the templating behaviour of Cu-TETA (222) and Cu-232 complexes contained within SAPO-34 and SAPO-18, respectively. EPR spectra were measured on as-prepared samples in hydrated, dehydrated (170 °C for 10 hours under vacuum) and rehydrated (exposed to moist air for one week) forms. A similar series of measurements

was also carried out on the calcined and re-hydrated samples (Figure 9). These spectra are commonly dominated by *g*-anisotropy and hyperfine coupling to the Cu^{2+} nucleus while couplings to the ligand nitrogen atoms are unresolved. Spectra of as-prepared materials have been satisfactorily fitted using two different species whose axial *g*- and hyperfine tensor components are reported in Table S2. The spectra of the as-prepared samples have the characteristic profile of Cu^{2+} complexes in which the copper cation is surrounded by four planar nitrogen atoms, fitted with $g_{||}$ values of 2.17 - 2.22 and, $A_{||}$ 370 - 570 MHz, confirming that the Cu^{2+} is present as a complex (for comparison, a typical reported value is $g_{||}$ 2.212, $A_{||}$ 545 MHz. [23]) A small change in the spectrum of Cu-232 was recorded upon dehydration. This may be caused by the removal of axial water molecules from the coordination sphere of Cu^{2+} or by the tetragonal distortion of the complex possibly due to framework relaxation upon water loss; no effect was observed by UV-visible spectroscopy. The increase of $g_{||}$ from 2.198 to 2.206 and the simultaneous decrease of $A_{||}$ from 410 to 351 support the second of the two possibilities. [26] On subsequent exposure to air the signal reverted to that of the hydrated form and could be simulated with identical parameters.

The spectra of the calcined solids have been fitted using a combination of rhombic and isotropic species (Table S3). The spectra are consistent with the removal of polyamine ligands from the Cu^{2+} cations to give isolated Cu^{2+} cations dispersed throughout the pores, as seen previously for hydrated Cu-CHA ($g_{||}$ 2.325, $A_{||}$ 487 MHz) [27] and Cu-SAPO-18 ($g_{||}$ 2.389, $A_{||}$ 434 MHz) materials. [28]

3.3. Template removal and porosity

Selected samples have been calcined at 550 °C in a dry oxygen flow in order to remove the organic SDAs and release Cu^{2+} and Ni^{2+} cations within the pores of SAPO-34 and

SAPO-18. As Figure 10 shows, the crystallinity of the samples was not strongly affected by the detemplation process.

Nitrogen adsorption at -196 °C on calcined samples has been measured to investigate the effect of metal cations within SAPO-34 and SAPO-18 on their pore volume (Figure S4). N_2 uptakes at $p/p_o = 0.2$ corresponds to 5.2 mmol g^{-1} for Cu-SAPO-34, 6.3 mmol g^{-1} for Ni-SAPO-34, 5.1 mmol g^{-1} for Cu-SAPO-18 and 5.0 mmol g^{-1} for Ni-SAPO-18, indicating internal pore volumes of 0.18, 0.22, 0.18 and 0.17 cm^3 g^{-1}, respectively. These are lower than those measured for SAPO-34 (typically between 0.25 – 0.32 cm^3 g^{-1}), [29] which is attributed to the combined effect of space occupied by M^{2+}, additional mass of M^{2+} and the presence of non-porous amorphous material.

3.4. In situ synchrotron IR micro-spectroscopy: calcination of Ni-SAPO-18

The calcination in air of SAPO-18 containing Ni-232 has been followed *in situ* by microcrystal synchrotron IR absorption spectroscopy. Using the OPUS software suite [19] individual pseudo-cubic single crystals with an average length of 50 μm were carefully selected and measured. Samples were heated to 100 °C in order to remove weakly bound water, followed by heating further to 550 °C in 50 °C increments. Each temperature was kept constant for 10 minutes before the spectrum was recorded. The spectra collected between 100 and 300 °C include bands characteristic of the organic 1,2-bis(3-aminopropylamino)ethane (Figure 11). [30] The absorption bands are assigned as follows: 3334 and 3360 cm^{-1} N-H vibrational stretches (primary amines), 1600 cm^{-1} N-H_2 scissoring, 1272 cm^{-1} C-N stretch (primary amines), 3141 cm^{-1} N-H stretch (secondary amines), 1234 cm^{-1} C-N stretch (secondary amines), 2968 and 2890 cm^{-1} C-H stretches, 1464 cm^{-1} C-H bending or scissoring. At 350 °C the thermal

degradation of the polyamine results in changes in the spectra. Two new resonances appear at 1643 cm^{-1} (strong) and 2250 cm^{-1} (medium), assigned to C=N and C≡N stretches respectively. At 400 °C the degradation is more evident: all the characteristic N-H and C-H bands of the organic template disappear and the typical bands of the bridging hydroxyl groups that balance the overall framework charge appear at 3595 cm^{-1}. The remaining part of the spectrum is dominated by imine and nitrile signals. The broad band at 3342 cm^{-1} might be assigned to the N-H stretch of the $H_2C=N$ group. The organic structure-directing agent is completely removed by 550 °C, resulting in release of Ni^{2+} cations into the pore space of SAPO-18.

3.5. Solid-state NMR

Solid-state MAS NMR spectra were recorded on as-synthesised and calcined (dehydrated) SAPO-34 and SAPO-18-containing copper (Figure 12) and nickel (Figure S5). The ^{27}Al MAS NMR spectra of as-prepared samples show two resonances: one between 7.1–7.9 ppm assigned to five-fold Al and one between 36.4–37.5 ppm assigned to tetrahedrally coordinated Al atoms. For Ni-SAPO-34 and Cu-SAPO-18, the five-fold environment is more abundant. Due to the absence of water in the dehydrated samples, the additional coordination is likely to be from charge-balancing hydroxyl groups or from the ligand. This is supported by the disappearance of the corresponding resonance after calcination (a very small shoulder is still present in Cu-SAPO-18). The ^{31}P MAS NMR spectra of the as-prepared samples show one resonance around -28 ppm characteristic of tetrahedrally coordinated P atoms bound via O atoms to four Al atoms ($P(OAl)_4$). Only the spectrum of Cu-SAPO-18 has been affected by the template removal: a small shoulder appeared around -17 ppm. The ^{29}Si MAS NMR spectra of as-prepared samples show only one peak in the range between -90.4 and -91.4 ppm,

corresponding to $Si(OAl)_4$, which indicates that the Si mainly substitutes for P in the framework. This results in a distribution of negative charge over the framework, which has been shown to enhance the stability of extra-framework Cu^{2+} cations in the NH_3 SCR of NO. [11] The $Si(OAl)_4$ resonances are shifted ca. 5 ppm upfield upon calcination.

3.6. Location of Cu^{2+} and Ni^{2+} within calcined and dehydrated SAPO-34 and SAPO-18 by Rietveld refinement

Following calcination, the metal cations are released into the cavities of SAPO-34 and SAPO-18. Rietveld refinement and Fourier analysis were used to locate copper within Cu-SAPO-34 and Cu-SAPO-18 prepared using Cu(HEEDA) and Cu-232 as SDAs, respectively, as described in Table 4. These samples were chosen because they had high Cu^{2+} contents and good crystallinity. Crystallographic data are listed in Table 4 while the refinement plots and crystal structures are shown in Figures 13 and 14. The final atomic coordinates and thermal parameters for Cu-SAPO-34 and Cu-SAPO-18 are listed in Table S4 and S6, respectively. Selected interatomic lengths and angles are summarised in Tables S5 and S7.

In SAPO-34, Cu^{2+} cations were located within the *cha* cage at an average distance of 2.56(3) Å from the framework oxygen atoms of the 8R window with a fractional site occupancy of 0.16 (Figure 14a). Combining the refined occupancy with its site multiplicity suggests 1.4 Cu^{2+} cations per unit cell, corresponding to 0.47 cations in each of the three *cha* cages. In SAPO-18, Cu^{2+} cations were located in the centre of the 6Rs of the D6R sub-units of the AEI structure at an average distance of 2.24(5) Å and 2.28(3) Å from the framework oxygen atoms, with a fractional site occupancy of 0.15

(Figure 14b). Combining the refined occupancy with site multiplicity suggests 1.2 Cu^{2+} cations per unit cell, corresponding to 0.3 Cu^{2+} cations in each of the four *aei* cages.

Details of the refinement and structures of calcined Ni-SAPO-34 and Ni-SAPO-18 are reported in the Supplementary Information (Tables S8, Figures S6 and S7). In Ni-SAPO-34, two sites were determined for the extra-framework Ni^{2+}, within the *cha* cage at an average distance of 2.22(2) Å from the framework oxygen atoms of the 8R window (fractional site occupancy of 0.11) and at the centre of the six-member rings (6Rs) at an average distance of 2.16(4) Å from the framework oxygen atoms (fractional occupancy 0.09). For Ni-SAPO-18, Ni^{2+} was located in the centre of the 6Rs of the D6R sub-units. The final atomic coordinates and thermal parameters for Ni-SAPO-34 and Ni-SAPO-18 are listed in Table S9 and S11, respectively. Selected interatomic lengths and angles are summarised in Tables S10 and S12.

3.7. Catalytic performances of copper-containing catalysts in the selective catalytic reduction of NO

Cu-SAPO-34 and Cu-SAPO-18 samples prepared by the one-pot method using Cu-TETA and Cu-232/TEA^+ in the gels (see Table 1) were tested as catalysts for the selective catalytic reduction of NO_x by NH_3. Cu-SAPO STA-7 prepared by the one-pot route reported by Picone *et al*. [6] was also tested, and is a suitable comparison because the framework structure is closely related to that of SAPO-34 and SAPO-18 (D6Rs as building units and each cage linked to six others by 8R windows). The chemical composition, particle sizes (8 – 10 μm), morphology, and BET surface area of all catalyst samples tested are given in Table 5.

The catalytic conversion of NO upon reduction by NH_3 is shown as a function of reaction temperature (Figure 15). The full conversion of NO_x occurs by 230, 280 and 300 °C for Cu-SAPO-18, Cu-SAPO-34 and Cu-SAPO STA-7, respectively. All samples showed ca. 100% NO_x conversion in a window of temperature between ca. 300 and 430 °C. Hydrothermal aging at the elevated temperature of 900 °C deactivates Cu-SAPO-34 and Cu-SAPO-18 while it has less of an effect on Cu-SAPO STA-7, for which the NO_x conversion remains above 85%. In order to understand the possible causes of this drastic reduction in NO_x conversion, PXRD patterns from hydrothermally-aged samples were collected (Figure S8). SAPO-34 and SAPO-18 powder patterns have been fully replaced by a crystalline phase isostructural with tridymite, indicating that the frameworks of SAPO-18 and SAPO-34 prepared in this way collapse under these harsh conditions. The STA-7 framework remains partly intact. No formation of copper oxides or copper aluminates was detected.

3.8. Discussion

The results show that it is possible to perform the one-pot synthesis of Cu-SAPO-34 and Cu-SAPO-18 precursors to deNOx catalysts using a wider range of copper-polyamine complexes than previously reported, but that the choice of polyamine has an important influence on both the amount of Cu^{2+} incorporated and the type of zeotype structure that crystallises. The work targeted the synthesis of Cu-SAPOs, because of their relevance to selective catalytic reduction, but investigation of one-pot synthesis using Ni^{2+} polyamine complexes gives additional insight into the influence of the SDA-complex on the crystallisation phase selectivity.

PXRD shows that Cu-containing SAPO-34 are prepared using TETA, TEPA, PEHA, 323, DETA and HEEDA as SDAs, without the addition of further templating agents such as amines or quaternary ammonium salts. For the last four of these SDAs this was their first use in these reactions. It is also possible to prepare Cu-SAPO-18, using Cu-232 and TEA^+ as co-SDAs, over a narrow range of conditions. Using Ni^{2+} in place of Cu^{2+} in the syntheses resulted in the preparation of Ni-SAPO-34 and Ni-SAPO-18 for the first time. While the use of Ni^{2+} in the presence of TEPA, 323, DETA and HEEDA gives SAPO-34, the Ni-232 and Ni-TETA are effective templates for SAPO-18. UV-visible spectroscopy of the as-prepared solids gives important indications to the coordination geometry of the metal complex SDAs (Figures 5 and 6). For Cu^{2+} complexes, additional complementary information was available from EPR spectroscopy (Figure 9). Cu^{2+} and Ni^{2+} complexes with 232 tended to favour the crystallisation of SAPO-18, and in the light of the spectroscopic data this was investigated by computer modelling.

Chemical analysis shows (Table 2) significant Cu^{2+} content (0.27 – 0.30 Cu^{2+} per *cha* or *aei* cage) in all materials except those prepared in the presence of 323. For the latter case, this is likely to be due to weaker cation complexation under the conditions of the synthesis. For the Cu-SAPO-34 samples containing DETA and HEEDA, the Cu^{2+} is thought to be complexed by two molecules of each, octahedrally-coordinated. The Ni-SAPOs prepared with these SDAs also show UV-visible spectra characteristic of octahedrally-coordinated Ni^{2+}. Heating at 170 °C (Figures 5 and 6) has no effect on the Ni-DETA, Ni-HEEDA or Cu-DETA spectra, suggesting the coordination stays the same, but it appears that the coordination of the Cu-HEEDA alters, possibly due to a change in coordination of the hydroxyl O atoms to the Cu^{2+}. For the TETA, TEPA and PEHA, the included Cu^{2+} complexes show similar absorption maxima suggesting

octahedral coordination (Figure 5) which do not change strongly upon heating, except for an increase of species absorbing at 350 nm. Cu^{2+} EPR of Cu TETA likewise shows little change upon dehydration, indicating additional ligands bound strongly to the cation are not readily removed. Similar behaviour is observed by UV-visible spectroscopy (Figure 6) of the Ni^{2+} complexes of TEPA and PEHA in Ni-SAPO-34, but Ni-TETA undergoes a partial octahedral-to-square planar change in coordination geometry upon dehydration, which may be due to the higher relative stability of square planar Ni^{2+} complexes.

The Cu-232 complex has a distinctly different UV-visible spectrum, which correlates with crystallisation of SAPO-18 rather than SAPO-34. The UV-visible absorption spectrum suggests a Cu^{2+} coordination geometry approaching square planar. No change is observed in the UV-visible upon dehydration at 170 °C, but the EPR is more sensitive. Further work is required to understand this. The Ni-232 SDA also shows a different absorption spectrum in Ni-SAPO-18 from those of Ni-SAPO-34 that indicates both octahedral and square planar geometries are present, with the amount of square planar Ni^{2+} increasing upon heating. Taken together, these spectroscopic results indicate that a square planar geometry (or more specifically one in which the four N atoms are arranged equatorially) favours SAPO-18. This is supported by modelling studies, where a square planar $[Ni(232)]^{2+}$ complex shows a good fit (and more favourable interaction energies) to the *aei* cage. A combination of spectroscopic and modelling studies therefore indicates the $[M(232)]^{2+}$ complex, M = Cu, Ni, is a good SDA for the AEI framework. The main difference between the method of one-pot synthesis of Cu-SAPO-18 in this work from that of Corma and co-workers [12] is that whereas a template, N,N-dimethyl-3,5-dimethylpiperidinium, is used in that work to direct the synthesis of

the SAPO-18, entraining Cu^{2+} and/or Cu^{2+} complex at the same time, in our synthesis it is the Cu-232 complex that directs crystallisation of the AEI structure.

In all of the solids prepared here by the one-pot method, calcinations gives crystalline, microporous solids. Their pore volumes are lower than those expected for the corresponding SAPOs without metal cations by ca. 30%. Solid state NMR indicates the frameworks of the calcined forms are fully tetrahedrally-coordinated, with the Si replacing P exclusively, and therefore imparting one negative charge per Si to the framework. This balances the positive charge of cations released by removal of the polyamines and has previously been shown to give rise to catalysts of good stability in the SCR reaction. [11] The mechanism of the template removal from Ni-SAPO-18 by calcination in air has been studied in detail by *in situ* single crystal SR IR spectroscopy. Thermal degradation of the polyamine begins at 350 °C and involves the formation of imine and nitrile groups. By 550 °C the organic SDA is completely removed with release of metal cations into the pores of SAPO-18. In the case of the Cu^{2+} SAPOs, EPR spectra show the change in environment of the Cu^{2+} cations upon calcination, corresponding to a release of the Cu^{2+} cations from the complex and their distribution within extra-framework sites of the zeotypes.

Rietveld refinement located Cu^{2+} cations in calcined Cu-SAPO-34 and Cu-SAPO-18 materials prepared using HEEDA and 232 in the synthesis. Here, Cu^{2+} cations in SAPO-34 were located only in the site near the 8R window of the *cha* cage. In previous studies of ion-exchanged Cu-SAPO-34, the Cu^{2+} cations were found displaced into the ellipsoidal cavity in front of the 6R of the D6R sub-units of the CHA structure by a combination of H_2 TPR (temperature-programmed reduction) and EPR techniques [31] and a similar site for Cu^{2+} cations was identified by Deka and co-workers [10] via

Rietveld refinement on a slightly intergrown calcined Cu-SAPO-34 (CHA/AEI) prepared using Cu^{2+}-TETA as SDA. For Cu-SSZ-13, the aluminosilicate version of SAPO-34, copper cations have been found in the site observed here and in other two sites: (i) in the center of the hexagonal prism [32] and (ii) in the plane and slightly off-centre of the D6R. [33]

For Cu-SAPO-18, Cu^{2+} cations were located in 6R sites in this work. Wasowicz et al. [28] reported a position similar to that found here for Cu^{2+} cations which they determined by EPR and ESEM on ion-exchanged and dehydrated Cu-SAPO-18. Their studies suggested the Cu^{2+} was positioned inside the pear-shaped *aei* cage slightly out of the plane of the 6R of the D6R subunits.

Measurement of the catalytic activity in the SCR of NO with NH_3 for selected samples of Cu-SAPO-34, Cu-SAPO-18 and, for comparison, the related Cu-SAPO STA-7, all prepared by one-pot synthesis, showed that all were active over a wide temperature range, giving 100% conversion under realistic conditions. Cu-SAPO-18 shows higher activity than the other two at low temperatures, and full conversion by 230 °C, rather than 300 °C for the other two. None of the materials is fully stable under the harsh hydrothermal conditions (900 °C), although Cu-SAPO STA-7 does retain some crystallinity and shows higher activity after treatment. Notably, Moliner et al. have recently reported that SAPO-34 [11] and SAPO-18 [12] prepared by one-pot routes are stable to hydrothermal aging at the lower temperature of 750 °C. More work is required to understand the mechanism of structural collapse under harsh hydrothermal treatment conditions in order to optimise the materials synthesis by controlling framework composition, copper content and the presence of structural intergrowths and other defects.

4. Conclusions

The one-pot synthesis route to Cu-SAPO-34, reported previously with triethylene-tetramine (TETA) and tetraethylenepentamine (TEPA), has been extended to the Cu-polyamine SDAs diethylenetriamine (DETA), N-(2-hydroxyethyl)ethylenediamine (HEEDA) and pentaethylenehexamine (PEHA). The use of complementary spectroscopic methods, in particular UV-visible and EPR spectroscopy, confirm Cu^{2+} is complexed within as-prepared SAPO-34, octahedrally-coordinated. By contrast, the use of N,N′-bis(2-aminoethyl)-1,3-propanediamine (232), in the presence of tetraethylammonium hydroxide, favours the crystallisation of Cu-SAPO-18 with included Cu-232, while the addition of 1,2-bis(3-aminopropylamino)ethane (323) does not lead to the inclusion of complexed Cu^{2+}. Analysis of the products of a parallel series of syntheses using Ni^{2+} complexes of the same polyamines give additional insight into the templating action of these SDAs, and particularly the selectivity to the SAPO-18 using metal complexes of 232. Modelling suggests the equatorially-coordinated tetramine fits the *aei* cage closely.

Calcination of the as-prepared Cu-SAPO-34 and Cu-SAPO-18 liberates Cu^{2+} cations into extra-framework cation sites. As expected, selected calcined Cu-SAPO-18 and Cu-SAPO-34 materials (and a comparative Cu SAPO STA-7) are highly active for the selective catalytic reduction of NO with NH_3. The samples lose crystallinity and consequently activity upon hydrothermal treatment at 900 °C, so that additional work is required to improve their hydrothermal stability. Nevertheless, Cu-SAPO STA-7 does show some resistance to collapse, suggesting that careful control of composition and structure can improve the hydrothermal stability of these types of materials.

Acknowledgements

This work has been supported by Johnson Matthey PLC, UK. We acknowledge Diamond Light Source for time on beamline B22 under Proposals SM8875-1, Dr Gianfelice Cinque and Dr Paul Donaldson for their help and Prof. Russell Howe (University of Aberdeen) as Principal Investigator for the beamtime. Solid-state NMR spectra were obtained at the EPSRC UK National Solid-state NMR Service at Durham. We thank Mrs. Sylvia Williamson (St Andrews) for collection of TGA, AAS and N_2 adsorption isotherms and Mr. Stephen Boyer (London Metropolitan University) for Elemental Analysis.

References

[1] (a) P.G. Blakeman, E.M. Burkholder, H.-Y. Chen, J.E. Collier, J.M. Fedeyko, H. Jobson, R.R. Rajaram, Catal. Today, 231 (2014) 56–63. (b) D. Wang, L. Zhang, J. Li, K. Kamasamudram, W.S. Epling, Catal. Today, 231 (2014) 64–74. (b) I. Lezcano-Gonzalez, U. Deka, B. Arstad, A. Van Yperen-De Deyne, K. Hemelsoet, M. Waroquier, V. Van Speybroeck, B.M. Weckhuysen, A.M. Beale, Phys. Chem. Chem. Phys., 16 (2014) 1639–1650. (c) M. Moliner, C. Franch, A.E. Palomares, M. Grill, A. Corma, Chem. Commun., 28 (2012) 8264–8266. (d) S.T. Korhonen, D.W. Fickel, R.F. Lobo, B.M. Weckhuysen, A.M. Beale, Chem. Commun., 47 (2011) 800–802. (e) J.H. Kwak, R.G. Tonkyn, D.H. Kim, J. Szanyi, C.H.F. Peden, J. Catal. 275 (2010) 187–190. (f) I. Bull, R.S. Boorse, W.M. Jaglowski, G.S. Koermer, A. Moini, J.A. Patchett, W.M. Xue, P. Burk, J.C. Dettling, M.T. Caudle, U.S. Patent 0,226,545, 2008.

[2] S.I. Zones, U.S. Patent 4,544,538, 1985.

[3] P. Wagner, S.I. Zones, M.E. Davis, R.C. Medrud, Angew. Chem. Int. Ed., 38 (1999) 1269–1272.

[4] B.M. Lok, C.A. Messina, R.L. Patton, R.T. Gajek, T. R. Cannan, E.M. Flanigen, J. Am. Chem. Soc., 106 (1984) 6092–6093.

[5] J.S. Chen, J.M. Thomas, P.A. Wright, R.P. Townsend, Catal. Lett., 28 (1994) 241–248.

[6] A.L. Picone, S.J. Warrender, A.M.Z. Slawin, D.M. Dawson, S.E. Ashbrook, P.A. Wright, S.P. Thompson, L. Gaberova, P.L. Llewellyn, B. Moulin, A. Vimont, M. Daturi, M.B. Park, S.K. Sung, I.-S Nam, S.B. Hong, Microporous Mesoporous Mater., 146 (2011) 36–47.

[7] L. Ren, L. Zhu, C. Yang, Y. Chen, Q. Sun, H. Zhang, C. Li, F. Nawaz, F.-S. Xiao, Chem. Commun., 47 (2011) 9789–9791.

[8] L. Ren, Y. Zhang, S. Zeng, L. Zhu, Q. Sun, H. Zhang, C. Yang, X. Meng, X. Yang, F.-S. Xiao, Chinese J. Catal., 33 (2012) 92–105.

[9] R. Martínez-Franco, M. Molinera, C. Franch, A. Kustov, A. Corma, Appl. Catal., B, 127 (2012) 273–280.

[10] U. Deka, I. Lezcano-Gonzalez, S.J. Warrender, A.L. Picone, P.A. Wright, B.M. Weckhuysen, A.M. Beale, Microporous Mesoporous Mater., 166 (2013) 144–152.

[11] R. Martínez-Franco, M. Moliner, P. Concepcion, J.R. Thogersen, A. Corma, J. Catal., 314 (2014) 73–82.

[12] R. Martínez-Franco, M. Moliner, A. Corma, J. Catal., 319 (2014) 36–43.

[13] E.C.V. Eschenroeder, A. Turrina, A.L. Picone, G. Cinque, M.D. Frogley, P.A. Cox, R.F. Howe, P.A. Wright, Chem. Mater., 26 (2014) 1434–1441.

[14] R. Garcia, I.J. Shannon, A.M.Z. Slawin, W. Zhou, P.A. Cox, P.A. Wright, Microporous Mesoporous Mater., 58 (2003) 91–104.

[15] R. Garcia, T.D. Coombs, M.J. Maple, W. Zhou, I.J. Shannon, P.A. Cox, P.A. Wright, Stud. Surf. Sci. Catal., 154 (2004) 993–1000.

[16] P. Cubillas, M. Castro, K.E. Jelfs, A. J.W. Lobo, B. Slater, D.W. Lewis, P.A. Wright, S.M. Stevens, M.W. Anderson**,** Crystal Growth & Design, 9 (2009) 4041–4050.

[17] S. Stoll, A. Schweiger, J. Magn. Reson., 178 (2006) 42–55.

[18] G. Cinque, M.D. Frogley, K. Wehbe, J. Filik, J. Pijanka, J. Synchr. Radiat. News, 24 (2011) 24–33.

[19] OPUS software 7.0, 2011, Bruker Optik GmbH, Germany.

[20] Materials Studio version 6.1, 2012, Accelrys Inc., San Diego, USA.

[21] (a) H.M. Rietveld, J. Appl. Crystallogr., 2 (1969) 2, 65–71. (b) A. Larson, R.B. von Dreele, General Structure Analysis System GSAS, Los Alamos National Laboratory, Los Alamos, NM, 2000. (c) B.H. Toby, J. Appl. Crystallogr., 34 (2001) 210–213.

[22] J.B. Hastings, W. Thomlinson, D.E. Cox, J. Appl. Crystallogr., 17 (1984) 85–95.

[23] (a) T. Sawada, K. Fukumaru, H. Sakurai, Biochem. Biophys. Res. Commun., 216 (1995) 154–161. (b) T. Sawada, K. Fukumaru, H. Sakurai, Chem. Pharm. Bull., 44 (1996) 1009–1016.

[24] D.J. Szalda, E. Fujita, R. Sanzenbacher, H. Paulus, H. Elias, Inorg. Chem., 33 (1994) 5855–5863.

[25] (a) C.K. Jørgensen, Acta Chem. Scand., 11 (1957) 399–400. (b) A.B.P. Lever, Inorganic electronic spectroscopy, Studies in Physical and Theoretical Chemistry, Elsevier 1984, 507. (c) Y. Dong, G.A. Lawrance, L.F. Lindoy, P. Turner, J. Chem. Soc., Dalton Trans., 8 (2003) 1567–1576.

[26] H. Yokoi, A.W. Addison, Inorg. Chem., 16 (1977) 1341–1343.

[27] A. Godiksen, F.N. Stappen, P.N.R. Vennestrøm, F. Giordanino, S.B. Rasmussen, L.F. Lundegaard, S. Mossin, J. Phys. Chem. C, 118(40) (2014) 23126−23138.

[28] T. Wasowicz, S.J. Kim, S.B. Hong, L. Kevan, J. Phys. Chem., 100 (1996) 15954−15960.

[29] (a) G. Qi, Z. Xie, W. Yang, S. Zhong , H. Liu, C. Zhang, Q. Chen, Fuel Process. Technol., 88 (2007) 437–441. (b) Q. Sun, N. Wang, D. Xi, M. Yang, J. Yu, Chem. Commun., 50 (2014) 6502–6505.

[30] S. Kinugasa, K. Tanabe, T. Tamura, Spectral Database for Organic Compounds, SDBS ; National Institute of Advanced Industrial Science and Technology (AIST): Japan, 2009. Available online at: http://riodb01.ibase.aist.go.jp/sdbs/cgi-bin/cre_index.cgi?lang=eng, SDBS No.: 21534.

[31] J. Xue, X. Wang, G. Qi, J. Wang, M. Shen , W. Li, J. Catal., 197 (2013) 56–64.

[32] (a) D.W. Fickel, R.F. Lobo, J. Phys. Chem. C, 114 (2010) 1633–1640. (b) J.H. Kwak, H. Zhu, J.H. Lee, C.H.F. Peden, J. Szanyi, Chem. Commun., 48 (2012) 4758–4760.

[33] U. Deka, A. Juhin, E.A. Eilertsen, H. Emerich, M.A. Green, S.T. Korhonen, B.M. Weckhuysen, A.M. Beale, J. Phys. Chem. C, 116 (2012) 4809−4818.

Tables

Table 1. Synthesis from gel composition 1.0 $Al(OH)_3$: 0.61 H_3PO_4 : 0.2 SiO_2 : 40 H_2O : 0.06 Cu^{2+} (0.1 Ni^{2+}): 0.2 polyamine.

Table 2. Composition of the samples (EDX, TGA, AAS and elemental analyses).

Table 3. Wavelengths of maxima in UV-visible spectra for hydrated and dehydrated Cu^{2+} and Ni^{2+} polyamine complexes within SAPO-34 and SAPO-18.

Table 4. Crystallographic data for calcined and dehydrated Cu-SAPO-34 and Cu-SAPO-18.

Table 5. Properties of copper-containing catalysts investigated for NO SCR.

Scheme

Scheme 1. Linear polyamines used as chelating agents with Cu^{2+} and Ni^{2+}.

Figures

Figure 1. Crystal structure and orientation of the double six-membered-ring units in CHA (a), (b) and AEI (c), (d), respectively.

Figure 2. PXRD patterns of as-prepared SAPOs obtained using Cu complexes, compared with simulated patterns.

Figure 3. PXRD patterns of as-prepared SAPOs obtained using Ni complexes compared with simulated patterns.

Figure 4. SEM of as-prepared Cu-, Ni- SAPO-34 (a, b) and SAPO-18 (c, d).

Figure 5. Solid-state UV-visible spectra for hydrated (solid line) and dehydrated (dashed line) copper complexes contained within SAPO-34 or SAPO-18.

Figure 6. Solid-state UV-visible spectra for hydrated (solid line) and dehydrated (dashed line) nickel complexes contained within SAPO-34 or SAPO-18.

Figure 7. Representation of *cha* (left) and *aei* (right) cages.

Figure 8. Energy-minimised positions of (two views of each) $[Ni\text{-}232]^{2+}$ (left) and $[Ni(DETA)_2]^{2+}$ (right) complexes within *cha* (above, a, b) and *aei* (below, c, d) cages. Framework grey, C black, H pink, N cyan, Ni^{2+} green).

Figure 9. EPR spectra of as-prepared Cu-TETA (a) and Cu-232 (b) contained within SAPO-34 and SAPO-18, respectively. In each of figure a and b, the bottom spectra are of as-prepared materials, the middle spectra are of the dehydrated (170 °C) materials, and the top spectra are of the re-hydrated solids. EPR spectra of calcined and hydrated Cu-SAPO-34 (c) and Cu-SAPO-18 (d). Solid line: experimental, dashed line: simulated.

Figure 10. PXRD patterns of calcined Cu-SAPO-34 (Cu-HEEDA) a, Ni-SAPO-34 (Ni-DETA) b, Cu-SAPO-18 (Cu-232, TEAOH) c and Ni-SAPO-18 (Ni-232) d.

Figure 11. Microcrystal infrared spectra measured during *in situ* calcination of one Ni-SAPO-18 crystal obtained using Ni-232 as the SDA.

Figure 12. Solid-state MAS NMR spectra for dehydrated as-prepared (solid line) and calcined (dashed line) Cu-SAPO-34 (a) and Cu-SAPO-18 (b). ^{29}Si, (middle) ^{31}P and (bottom) ^{27}Al.

Figure 13. Rietveld plots for calcined, dehydrated Cu-SAPO-34 (a) and Cu-SAPO-18 (b). Observed data (red crosses), calculated fit (green line), and difference plot (purple line). Peak positions are marked in black in (a) while in (b) SAPO-18 peak markers are marked in black and SAPO-34 in red.

Figure 14. Structures of calcined Cu-SAPO-34 (a) and Cu-SAPO-18 (b) viewed down the *c*-axis showing all symmetry related positions of Cu^{2+} cations and down the *b*-axis showing the local environments of Cu^{2+} site. Note that only a small fraction of these sites is occupied. (Al light blue, P dark gray, O red, Cu blue).

Figure 15. Catalytic conversions of NO as a function of temperature over freshly calcined samples and after hydrothermal treatment (900 °C for 1 h). Cu-SAPO-34, (a) and (b); Cu-SAPO-18, (c) and (d); Cu-SAPO STA-7, (e) and (f). The gas composition was 350 ppm NO, 385 ppm NH_3, 10% O_2, 4.5% CO_2, 4.5% H_2O in N_2. Flow rate 1.3 L min^{-1}, WHSV 195 L $(g_{cat}\ h)^{-1}$.

Table 1

run n°	polyamine	metal	co-base	product (by XRD)
1[a]	DETA	Cu^{2+}	DETA	SAPO-34
2		Ni^{2+}		SAPO-34
3	HEEDA	Cu^{2+}	HEEDA	SAPO-34
4		Ni^{2+}		SAPO-34
5	TETA	Cu^{2+}	TETA	SAPO-34
6		Ni^{2+}		SAPO-18[d]
7[b]		Cu^{2+}	232	amorphous
8[c]	232		TEAOH	SAPO-18[d]
9		Ni^{2+}	232	SAPO-18[d]
10			TEAOH	intergrown CHA/AEI
11	323	Cu^{2+}	323	SAPO-34
12		Ni^{2+}		SAPO-34
13	TEPA	Cu^{2+}	TEPA	SAPO-34
14		Ni^{2+}		SAPO-34
15	PEHA	Cu^{2+}	PEHA	SAPO-34
16		Ni^{2+}		intergrown CHA/AEI

The crystallisation temperature, time and pH are 190 °C, 6 days and 7, respectively, unless otherwise stated: (a) 8 days; (b) 12 days.

(c) 1 wt% of STA-7 seeds added (with respect to SiO_2 content).

(d) Sample contains a small impurity of SAPO-34.

Table 2

polyamine	metal	co-base	product (by XRD)	unit cell composition (by EDX, AAS, TGA)	C /N (calc)	C / N (exp)
DETA	Cu^{2+}	DETA	SAPO-34	$[Cu\text{-}(DETA)_2]_{0.8}[DETA]_{2.5}$ $Al_{18}P_{14.2}Si_{3.8}O_{72}$ $11.1H_2O$	1.14	1.28
DETA	Ni^{2+}	DETA	SAPO-34	$[Ni\text{-}(DETA)_2]_1[DETA]_{0.9}$ $Al_{18}P_{14.1}Si_{3.9}O_{72}$ $9.0H_2O$	1.14	1.25
HEEDA	Cu^{2+}	HEEDA	SAPO-34	$[Cu\text{-}(HEEDA)_2]_{1.1}[HEEDA]_{2.2}$ $Al_{18}P_{14.5}Si_{3.5}O_{72}$ $4.5H_2O$	1.71	1.76
HEEDA	Ni^{2+}	HEEDA	SAPO-34	$[Ni\text{-}(HEEDA)_2]_{1.3}[HEEDA]_{1.7}$ $Al_{18}P_{14.3}Si_{3.7}O_{72}$ $7.8H_2O$	1.71	1.75
TETA	Cu^{2+}	TETA	SAPO-34	$[Cu\text{-}TETA]_{0.6}[TETA]_{2.6}$ $Al_{18}P_{15.5}Si_{2.5}O_{72}$ $11.3H_2O$	1.29	1.31
TETA	Ni^{2+}	TETA	SAPO-18	$[Ni\text{-}TETA]_{1.9}[TETA]_{2.2}$ $Al_{24}P_{19.2}Si_{4.8}O_{96}$ $8.2H_2O$	1.29	1.36
232	Cu^{2+}	TEAOH	SAPO-18	$[Cu\text{-}232]_{1.2}[232]_{1.8}[TEA^+]_{1.3}$ $Al_{24}P_{19.5}Si_{4.5}O_{96}$ $10.6H_2O$		2.01
232	Ni^{2+}	232	SAPO-18	$[Ni\text{-}232]_{2.5}[232]_{2.3}$ $Al_{24}P_{19}Si_5O_{96}$ $13.6H_2O$	1.50	1.55
232		TEAOH	intergrown CHA/AEI	N.D.[a]		
323	Cu^{2+}	323	SAPO-34	$Cu_{0.2}[323]_{2.1}Al_{18}P_{14.5}Si_{3.5}O_{72}$ $6H_2O$	1.71	1.72
323	Ni^{2+}	323	SAPO-34	$[Ni\text{-}(323)]_{1.0}[323]_{1.4}$ $Al_{18}P_{14.3}Si_{3.7}O_{72}$ $7.7H_2O$	1.71	1.66
TEPA	Cu^{2+}	TEPA	SAPO-34	$[Cu\text{-}TEPA]_{0.8}[TEPA]_{1.5}$ $Al_{18}P_{14.1}Si_{3.9}O_{72}$ $11.2H_2O$	1.37	1.36
TEPA	Ni^{2+}	TEPA	intergrown CHA/AEI	$[Ni\text{-}TEPA]_{1.4}[TEPA]_{1.1}$ $Al_{18}P_{14.4}Si_{3.6}O_{72}$ $4.6H_2O$[b]	1.37	1.41
PEHA	Cu^{2+}	PEHA	SAPO-34	$[Cu\text{-}PEHA]_{0.8}[PEHA]_{1.2}$ $Al_{18}P_{14.7}Si_{3.3}O_{72}$ $6H_2O$	1.43	1.43
PEHA	Ni^{2+}	PEHA	intergrown CHA/AEI	$[Ni\text{-}PEHA]_{1.4}[PEHA]_{0.8}$ $Al_{18}P_{14.3}Si_{3.7}O_{72}$ $3.1H_2O$[b]	1.43	1.45

The ratios Cu/Al 0.06 and Ni/Al 0.1 were used in all the preparations.
Approximation used for the determination of the chemical compositions: all the metal cations have been considered fully complexed by the ligands, except in the case of 323 with Cu^{2+}.
(a) N.D.: not determined.
(b) The chemical composition has been determined as pure SAPO-34.

Table 3

ligand	metal	λ_{max} hydrated	coordination geometry hydrated	colour	λ_{max} dehydrated	coordination geometry dehydrated	colour
DETA	Cu^{2+}	350 680	NA + O	light blue	350 680	NA + O	sky blue
	Ni^{2+}	350 530 900	O	fuchsia	350 530 900	O	fuchsia
HEEDA	Cu^{2+}	350 615	NA + dSP	blue	350 615	NA + dSP	blue yellow
	Ni^{2+}	350 530 620 900	O + P	violet	360 530 620 900	O + P	blue/violet
TETA	Cu^{2+}	602	dSP	light blue	612	dSP	light blue
	Ni^{2+}	350 530 900	O	pale green	350 445 620 900	SP + O	bright green
232 + TEA^{+}	Cu^{2+}	350 545	SP	lilac	350 545	SP	pale lilac
232	Ni^{2+}	350 445 550 620 900	O + SP	sand yellow	350 445 620 900	SP + O	sand yellow
323	Cu^{2+}	359	NA	grey	359	NA	yellow green
	Ni^{2+}	350 445 620	SP + O	pale yellow	350 445 620	SP + O + P	bright yellow
TEPA	Cu^{2+}	350 (660)	NA + O or P	blue	350 (660)	NA + O or P	blue
	Ni^{2+}	350 530 900	O	lilac	370 572 900	O (red shift)	blue
PEHA	Cu^{2+}	350 685	NA + O	light blue	350 685	NA + O	blue green
	Ni^{2+}	350 530 900	O	fuchsia	354 535 900	O	fuchsia

O octahedral, P pentacoordinate, SP square planar, dSP distorted square planar, NA not assigned.

Table 4

	Cu-SAPO-34[a]	**Cu-SAPO-18**[b]
Chemical composition[c]	$Cu_{1.4}H_{0.7}Al_{18}Si_{3.5}$ $P_{14.5}O_{72}$ 27.8H_2O	$Cu_{1.2}H_{2.1}Al_{24}Si_{4.5}$ $P_{19.5}O_{96}$ 36.3H_2O
Data collection		
Wavelength / Å	1.54056	1.54056
Diffractometer geometry	Debye-Scherrer	Debye-Scherrer
Sample	rotating 1.0 mm capillary	rotating 0.5 mm capillary
Scanned region / 2θ°	3.0 – 70.0	5.0 – 70.0
Step size / 2θ°	0.1	0.1
Unit cell		
Chemical formula	$Cu_{1.4}Al_{18}Si_{5.4}P_{12.6}O_{72}$	$Cu_{1.2}Al_{24}Si_6P_{18}O_{96}$
Space group	*R 3*	*C 1 2/c 1*
a / Å	13.7583(2)	13.7300(3)
b / Å	13.7583(2)	12.8139(4)
c / Å	14.9324(5)	18.6255(5)
β / °		90.061(7)
Volume / Å^3	2447.88(8)	3276.89(10)
Rietveld refinement		
Refined region / 2θ°	5.0 – 70.0	5.5 – 69.7
% of SAPO-34		17.5
R_{wp}	0.079	0.037
R_p	0.059	0.028
R_F^2	0.067	0.052
X^2	3.31	1.96

(a) Cu-SAPO-34 was prepared in the presence of Cu-$(HEEDA)_2$ as SDA SDA using the gel composition $Al(OH)_3$: 0.61 H_3PO_4 : 0.2 SiO_2 : 40 H_2O : 0.08 Cu^{2+} : 0.2 HEEDA (b) Cu-SAPO-18 was prepared in presence of Cu-232 and TEAOH as SDA using the gel composition reported in the experimental section.
(c) Determined combining EDX, TGA and AAS.
$R_{wp} = [\Sigma w_i(Y_{io} - Y_{ic})^2/\Sigma w_i Y_{io}^2]^{1/2}$; $R_p = \Sigma|Y_{io} - Y_{ic}|/\Sigma Y_{io}$; $R_F^2 = \Sigma|F_o^2 - F_c^2|/\Sigma|F_o^2|$; $\chi^2 = \Sigma w_i(Y_{io} - Y_{ic})^2/(N_{obs} - N_{var})$.

Table 5

catalyst	**Si / (Al + P + Si)**[a]	**Cu content wt%**[b]	**crystal shape, size**[c] **µm**	**BET**[d] **m^2 g^{-1}**
Cu-SAPO-34	0.107	2.53	rhombs, 8 - 10	339
Cu-SAPO-18	0.111	1.12	tetragonal prisms, 8 - 10	398
Cu-SAPO STA-7	0.104	1.56	tetragonal prisms, 8 - 10	335

(a) EDX.
(b) Atomic absorption.
(c) SEM.
(d) N_2 adsorption data.

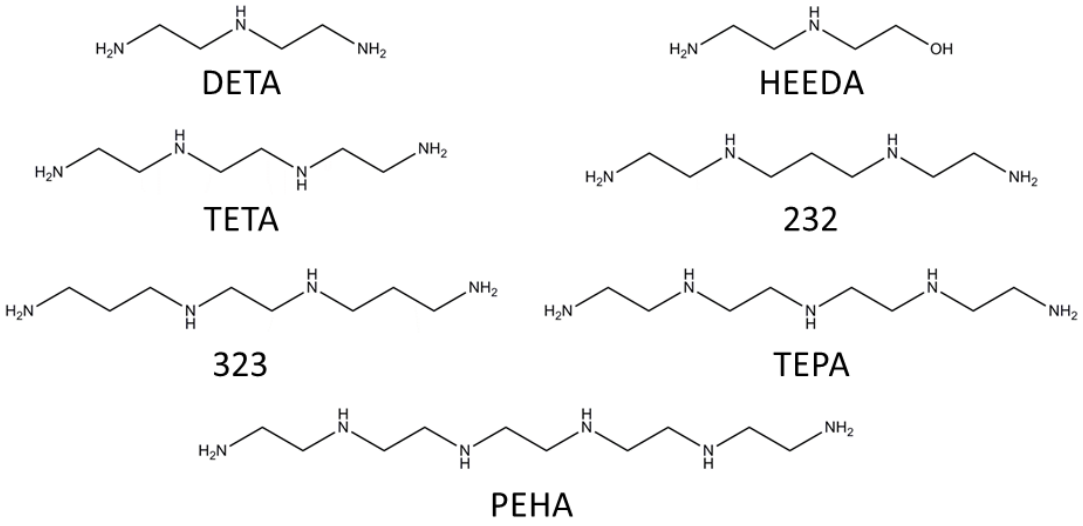

Scheme 1

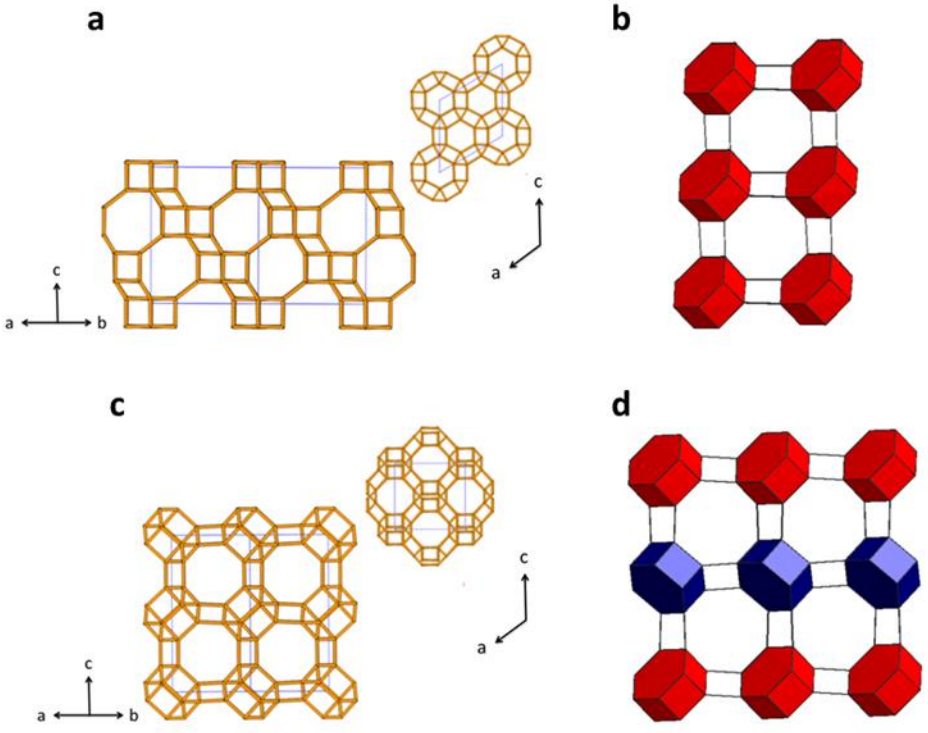

Figure 1

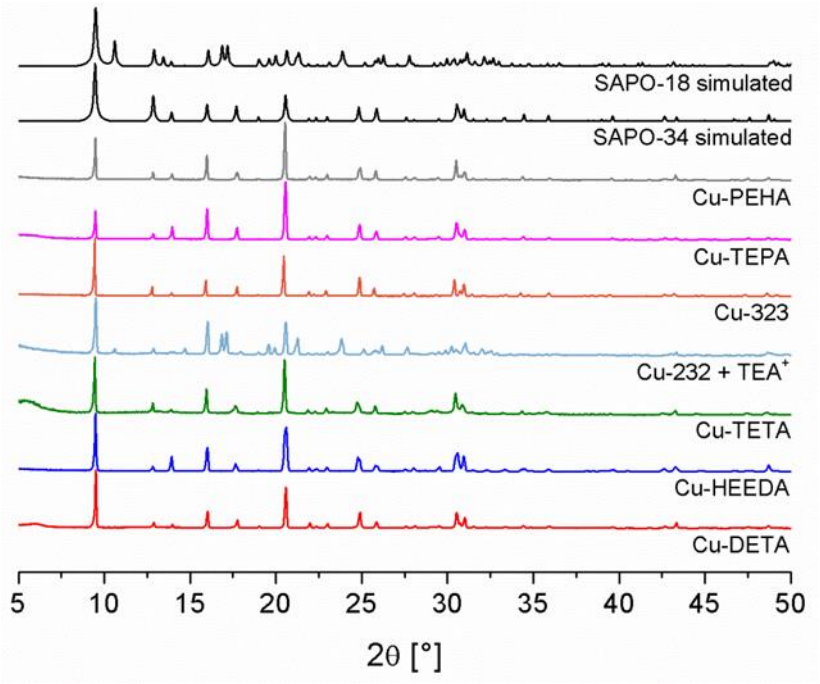

Figure 2

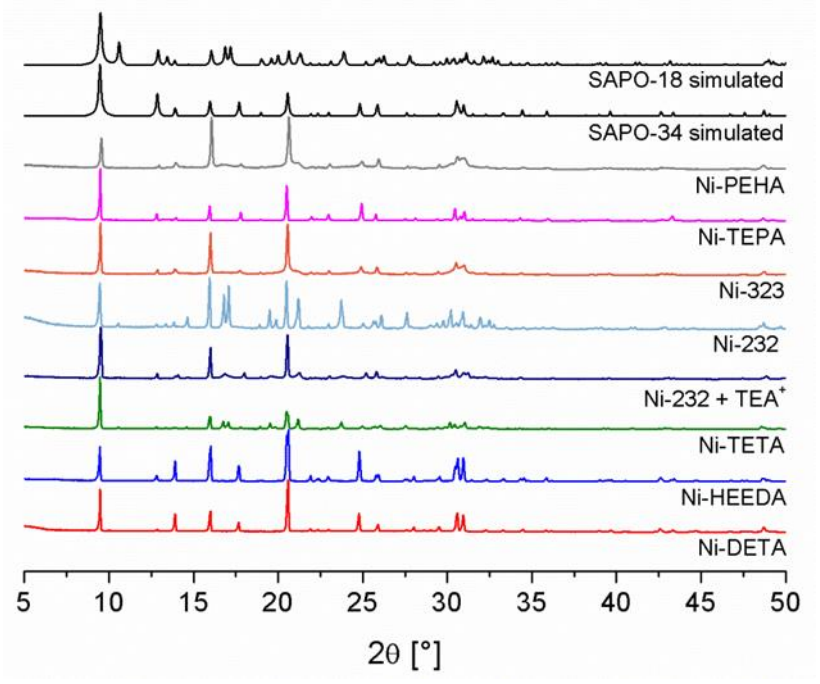

Figure 3

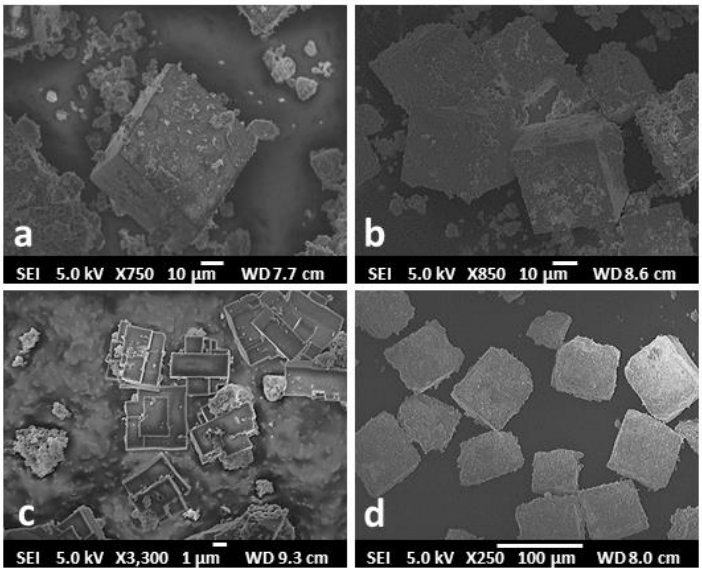

Figure 4

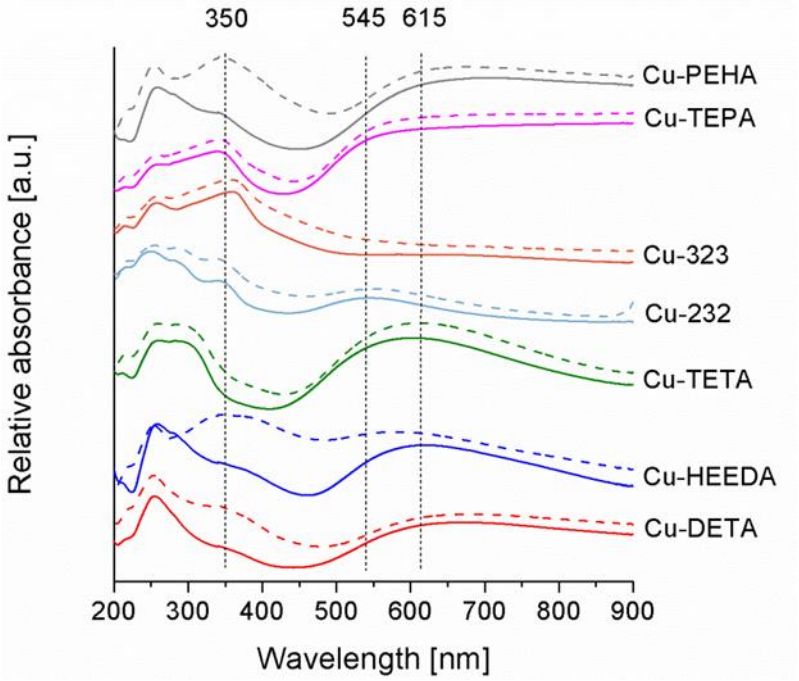

Figure 5

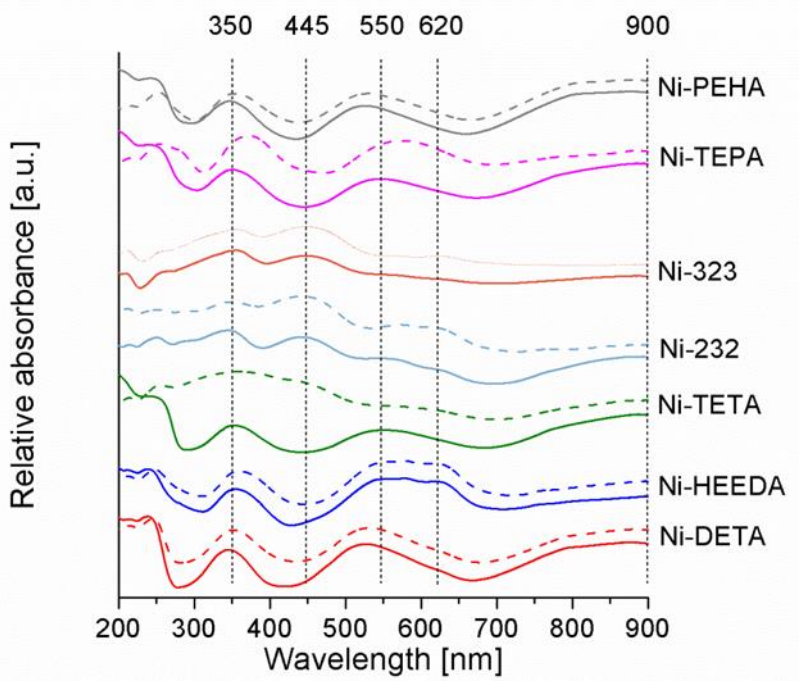

Figure 6

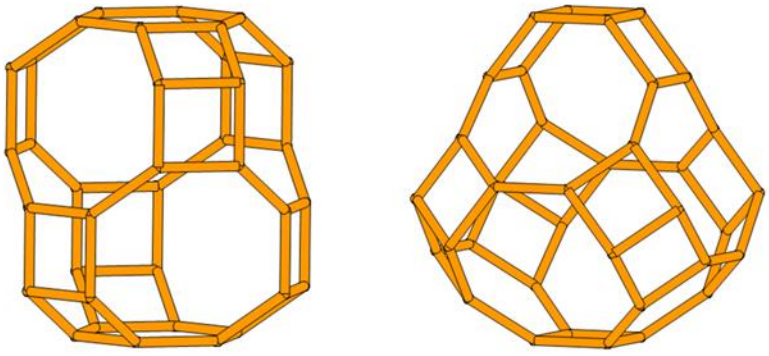

Figure 7

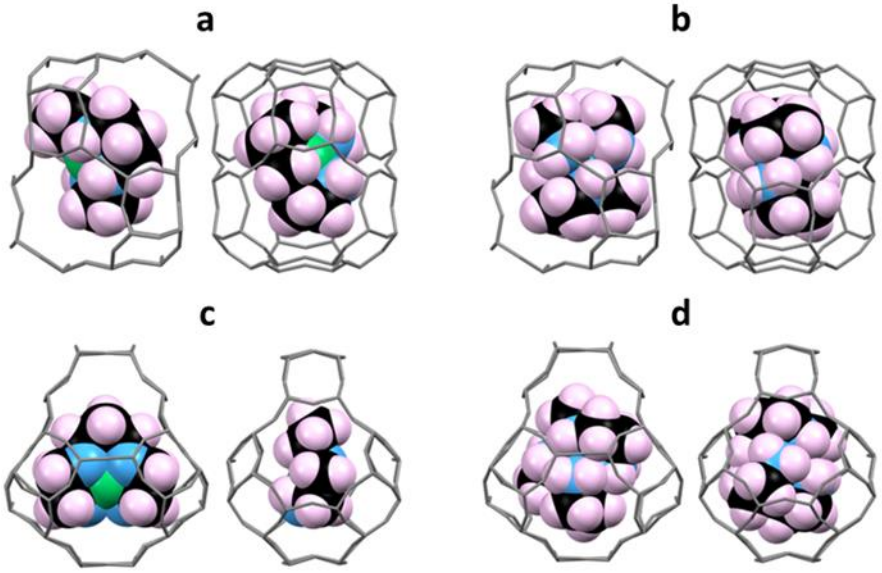

Figure 8

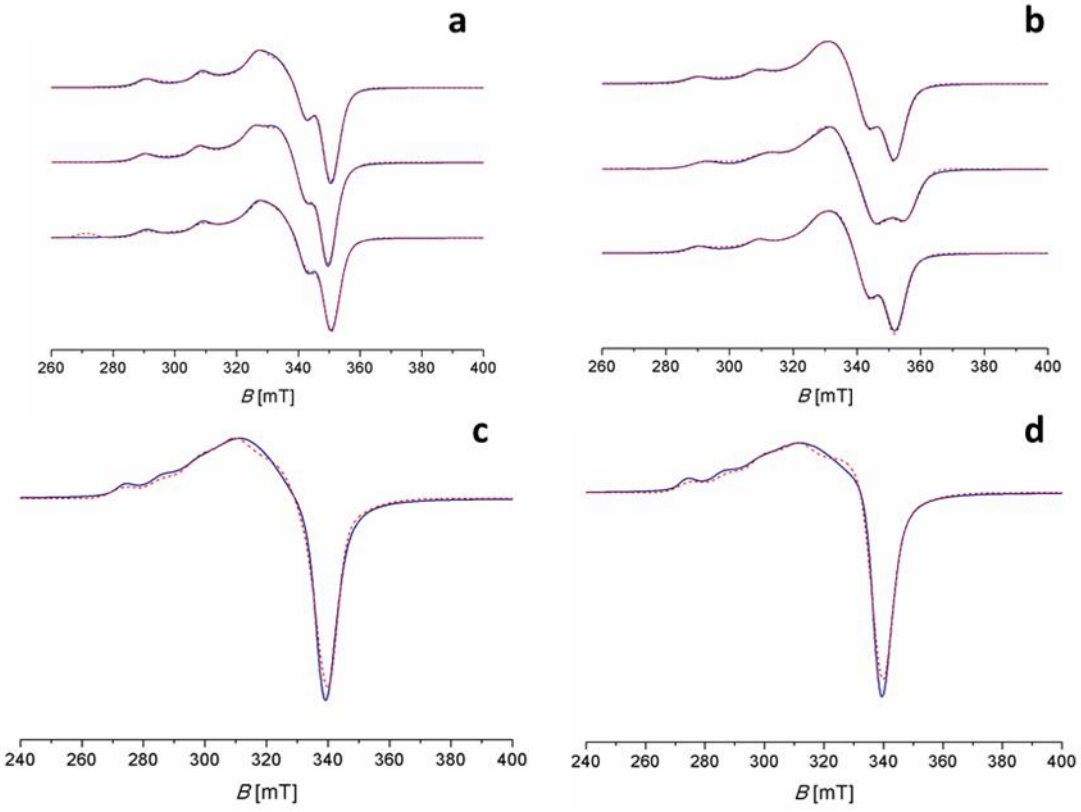

Figure 9

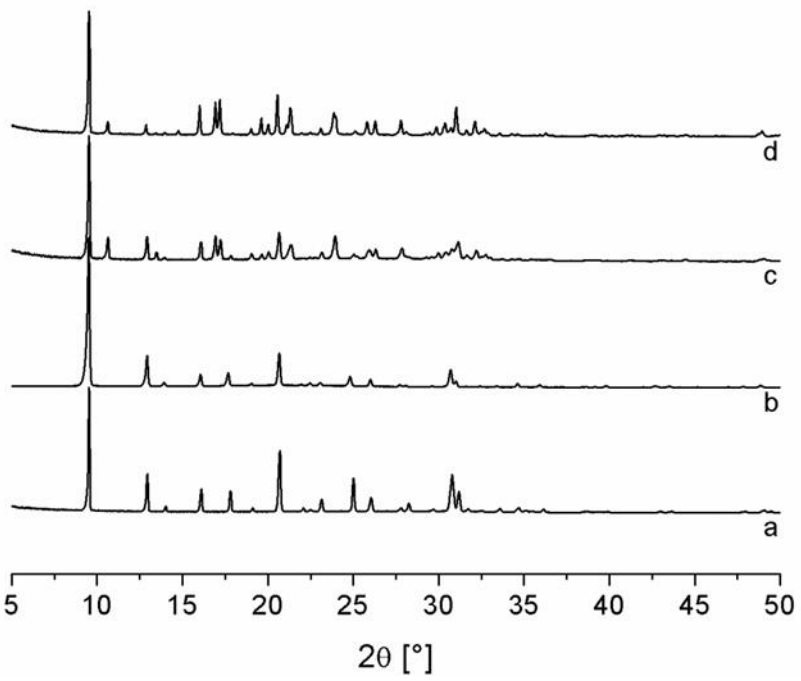

Figure 10

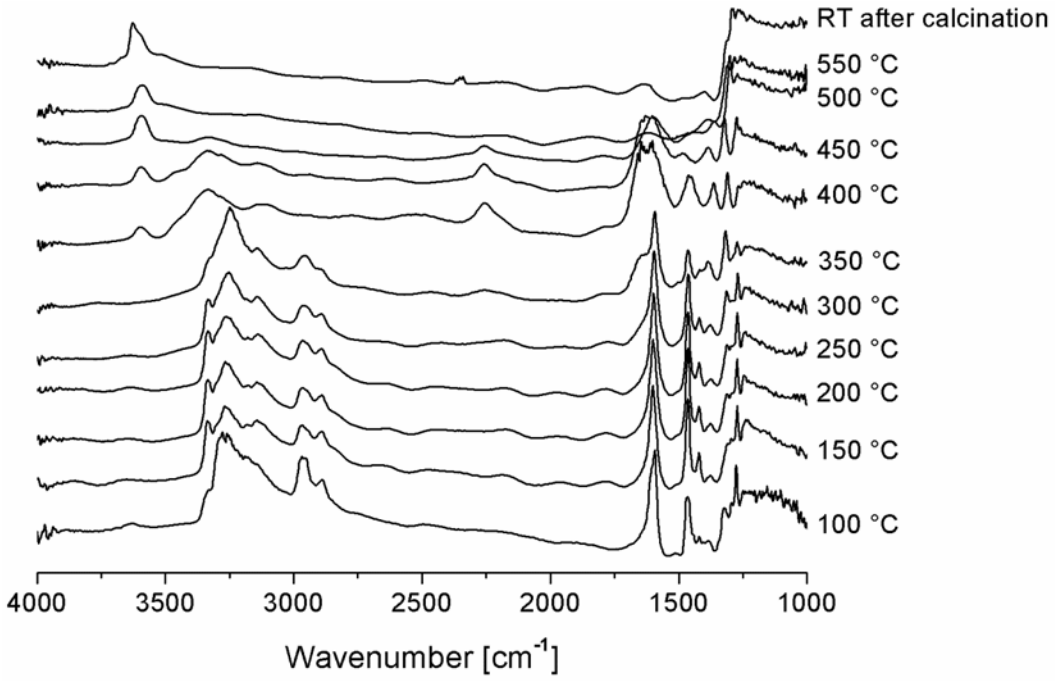

Figure 11

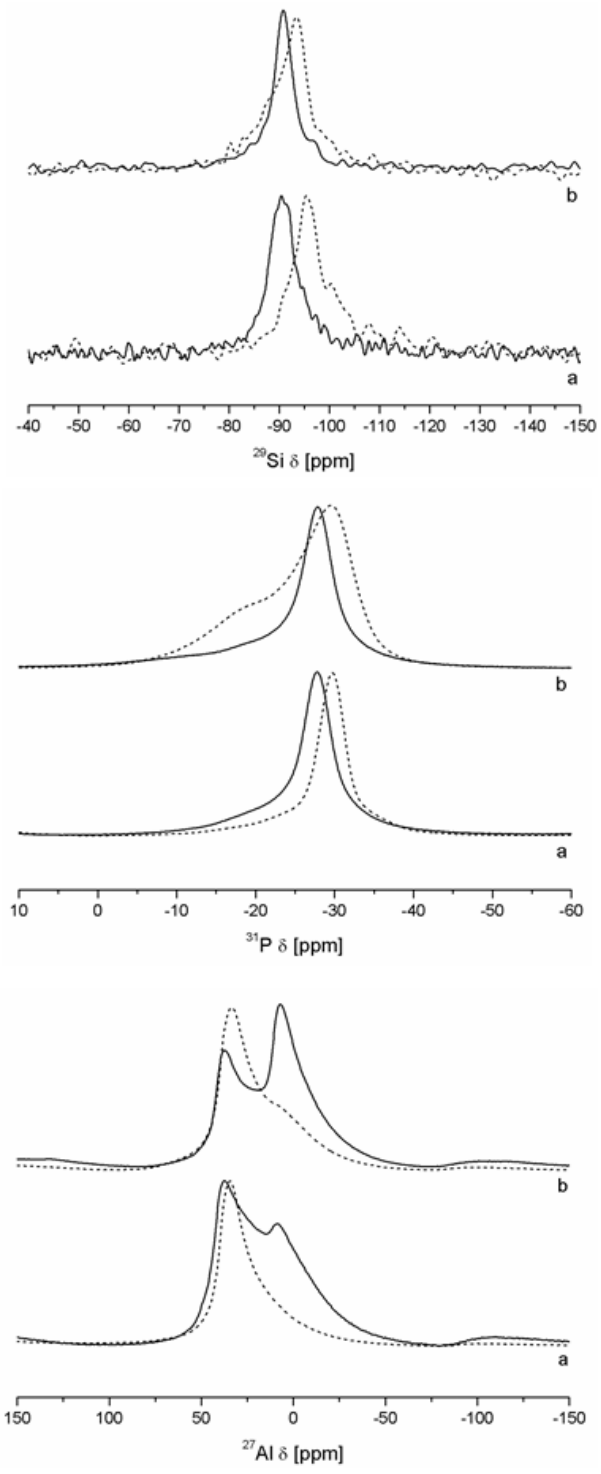
b
a
-40 -50 -60 -70 -80 -90 -100 -110 -120 -130 -140 -150
29Si δ [ppm]
b
a
10 0 -10 -20 -30 -40 -50 -60
31P δ [ppm]
b
a
150 100 50 0 -50 -100 -150
27Al δ [ppm]

Figure 12

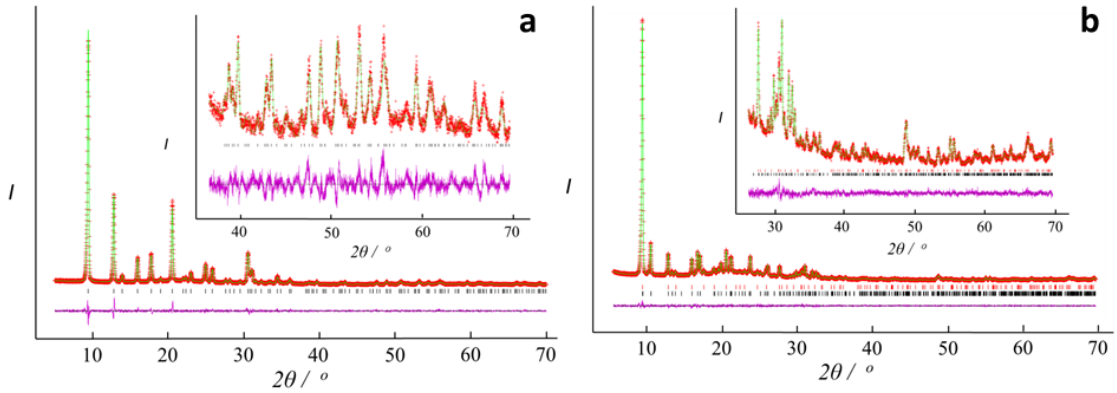

Figure 13

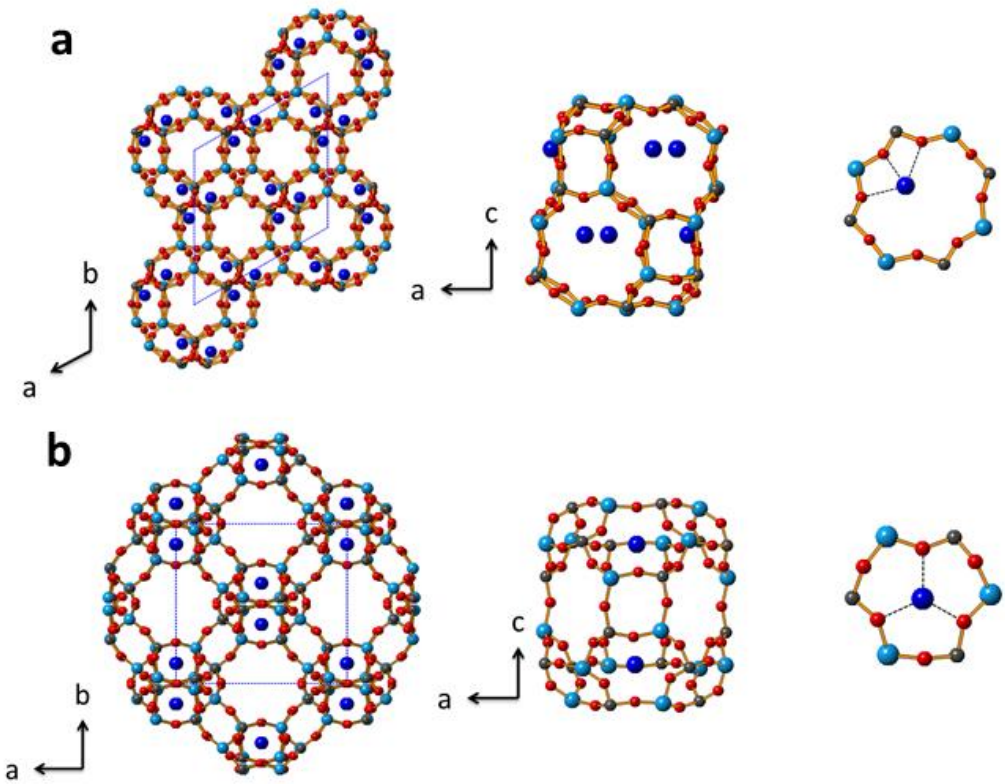

Figure 14

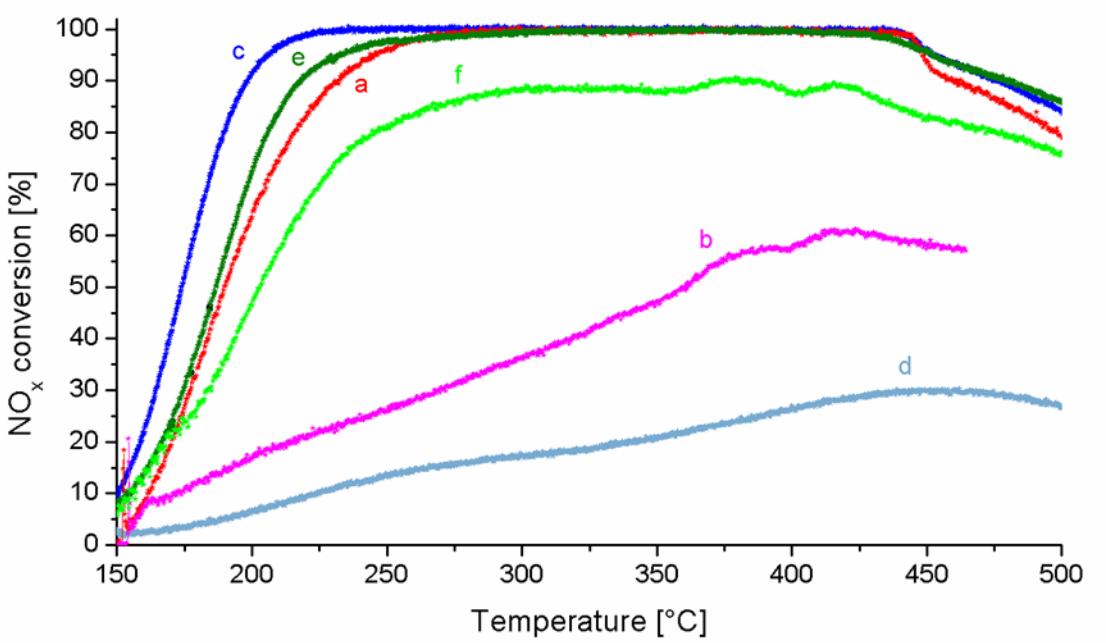
100
90
80
70
60
50
40
30
20
10
0
NOx conversion [%]
150
200
250
300
350
400
450
500
Temperature [°C]
c
e
a
f
b
d

Figure 15